

Science**A Structural Mechanism for MscS Gating in Lipid Bilayers**Valeria Vásquez, *et al.*
Science **321**, 1210 (2008);
DOI: 10.1126/science.1159674

The following resources related to this article are available online at www.sciencemag.org (this information is current as of October 17, 2008):

Updated information and services, including high-resolution figures, can be found in the online version of this article at:

<http://www.sciencemag.org/cgi/content/full/321/5893/1210>

Supporting Online Material can be found at:

<http://www.sciencemag.org/cgi/content/full/321/5893/1210/DC1>

A list of selected additional articles on the Science Web sites **related to this article** can be found at:

<http://www.sciencemag.org/cgi/content/full/321/5893/1210#related-content>

This article **cites 39 articles**, 20 of which can be accessed for free:

<http://www.sciencemag.org/cgi/content/full/321/5893/1210#otherarticles>

This article appears in the following **subject collections**:

Biochemistry

<http://www.sciencemag.org/cgi/collection/biochem>

Information about obtaining **reprints** of this article or about obtaining **permission to reproduce this article** in whole or in part can be found at:

<http://www.sciencemag.org/about/permissions.dtl>

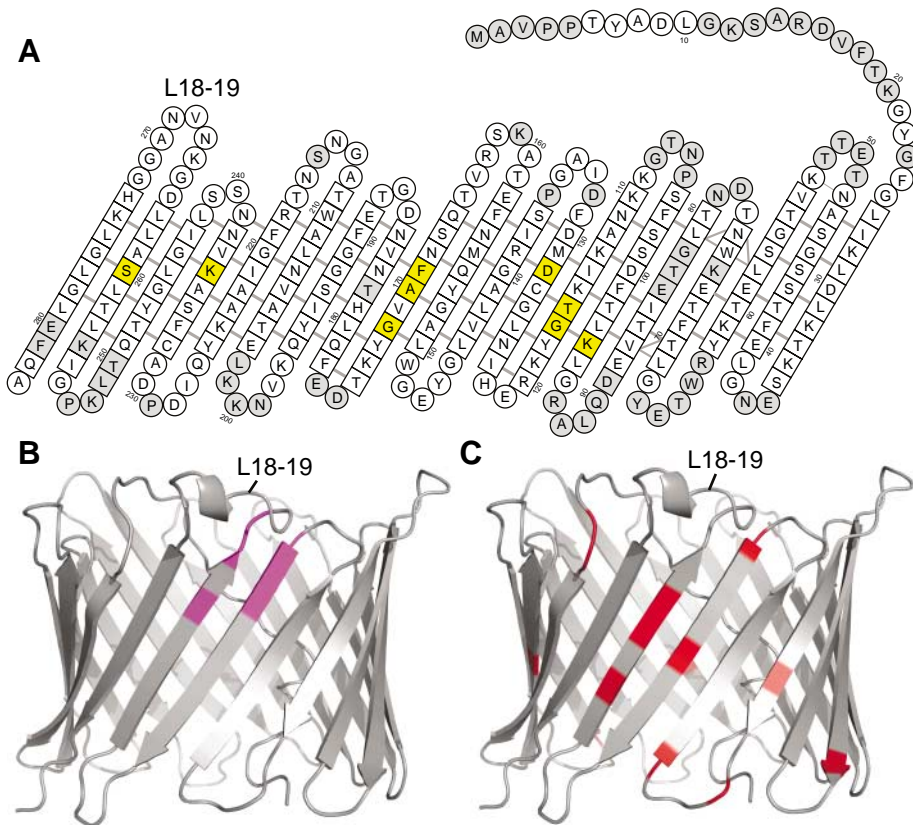


Fig. 4. Interactions of VDAC-1. In all three panels, the loop connecting strands 18 and 19 is indicated for orientation. **(A)** Residues with substantial chemical shift changes [$\Delta\delta(\text{HN}) > 0.05$ ppm] caused by cholesterol binding are shown in yellow (fig. S12). The amino acids of VDAC-1 are shown as in Fig. 1A. **(B)** Amide resonances of VDAC-1 with substantial chemical shift changes (fig. S13) caused by β -NADH are labeled magenta in this ribbon representation; all other residues are gray. **(C)** Residues involved in Bcl- x_L binding (13) are marked red in this ribbon representation; all other residues are gray.

22. M. K. Rosen *et al.*, *J. Mol. Biol.* **263**, 627 (1996).

23. K. Wüthrich, *NMR of Proteins and Nucleic Acids* (Wiley, New York, 1986).

24. S. H. White, *Membrane Proteins of Known 3D Structure*,

http://blanco.biomol.uci.edu/Membrane_Proteins_xtal.html (2008).

25. M. Forte, H. R. Guy, C. A. Mannella, *J. Bioenerg. Biomembr.* **19**, 341 (1987).
26. V. De Pinto *et al.*, *ChemBioChem* **8**, 744 (2007).
27. J. Song, C. Midson, E. Blachly-Dyson, M. Forte, M. Colombini, *Biophys. J.* **74**, 2926 (1998).
28. S. J. Schein, M. Colombini, A. Finkelstein, *J. Membr. Biol.* **30**, 99 (1976).
29. A. G. Komarov, B. H. Graham, W. J. Craigen, M. Colombini, *Biophys. J.* **86**, 152 (2004).
30. C. Hilty, G. Wider, C. Fernández, K. Wüthrich, *ChemBioChem* **5**, 467 (2004).
31. V. De Pinto, G. Prezioso, F. Thinnies, T. A. Link, F. Palmieri, *Biochemistry* **30**, 10191 (1991).
32. J. Song, C. Midson, E. Blachly-Dyson, M. Forte, M. Colombini, *J. Biol. Chem.* **273**, 24406 (1998).
33. J. V. Olsen *et al.*, *Cell* **127**, 635 (2006).
34. M. Colombini, *J. Membr. Biol.* **111**, 103 (1989).
35. V. De Pinto, R. Benz, F. Palmieri, *Eur. J. Biochem.* **183**, 179 (1989).
36. Single-letter abbreviations for the amino acid residues are as follows: A, Ala; C, Cys; D, Asp; E, Glu; F, Phe; G, Gly; H, His; I, Ile; K, Lys; L, Leu; M, Met; N, Asn; P, Pro; Q, Gln; R, Arg; S, Ser; T, Thr; V, Val; W, Trp; and Y, Tyr.
37. M. Zizi, M. Forte, E. Blachly-Dyson, M. Colombini, *J. Biol. Chem.* **269**, 1614 (1994).
38. PyMOL, <http://pymol.sourceforge.net>.
39. This work was supported by NIH roadmap grant GM075879. Purchase, operation, and maintenance of instruments used were supported by NIH grants GM066360, GM47467, and EB002026. S.H. was supported by the Swiss National Science Foundation. V.Y.O. was supported by the Wenner-Gren Foundation, Stockholm. Initial research on this project was supported by the Ludwig Foundation for Cancer Research. We thank V. Gelev from FBReagents.com, Cambridge, Massachusetts, for custom synthesis of the ^2H -LDAO; S. Samanta for help with the electrophysiological measurements; and D. Frueh, A. Koglin, Z.-Y. J. Sun, K. Oxenoid, and S. Jenni for technical help and valuable discussions. The atomic coordinates of VDAC-1 in LDAO micelles have been deposited at the Protein Data Bank with code 2k4t.

Supporting Online Material

www.sciencemag.org/cgi/content/full/321/5893/1206/DC1

Materials and Methods

Figs. S1 to S14

Table S1

References

3 June 2008; accepted 24 July 2008

10.1126/science.1161302

A Structural Mechanism for MscS Gating in Lipid Bilayers

Valeria Vázquez,^{1,2} Marcos Sotomayor,³ Julio Cordero-Morales,^{1,2} Klaus Schulten,⁴ Eduardo Perozo^{2*}

The mechanosensitive channel of small conductance (MscS) is a key determinant in the prokaryotic response to osmotic challenges. We determined the structural rearrangements associated with MscS activation in membranes, using functorial measurements, electron paramagnetic resonance spectroscopy, and computational analyses. MscS was trapped in its open conformation after the transbilayer pressure profile was modified through the asymmetric incorporation of lysophospholipids. The transition from the closed to the open state is accompanied by the downward tilting of the transmembrane TM1-TM2 hairpin and by the expansion, tilt, and rotation of the TM3 helices. These movements expand the permeation pathway, leading to an increase in accessibility to water around TM3. Our open MscS model is compatible with single-channel conductance measurements and supports the notion that helix tilting is associated with efficient pore widening in mechanosensitive channels.

Mechanosensation is involved in many physiological roles, including osmotic balance, touch, and hearing (1, 2). At the molecular level, mechanosensitivity relies on

the activity of ion channels that transduce a variety of mechanical stimuli to open a conductive pore. Mechanosensitive (MS) channels are grouped by function rather than sequence sim-

ilarity (3, 4). In prokaryotic systems, MS channels respond directly to bilayer deformations, with a transduction mechanism defined at the protein/lipid interface (5, 6). Although this is also true for some eukaryotic MS channels (7), many also respond to mechanical deformations through their association with the cytoskeletal network (8).

Although the molecular identification of eukaryotic MS channels remains challenging (2, 9, 10), the biophysical and structural properties of prokaryotic MS channels have proved far more tractable at the molecular level. The crystal structures for the MS channels of large (MscL) and small (MscS) conductance (11–13) have provided a molecular framework to interpret functional and biophysical data and have helped establish the basic mechanistic principles by which these two distinct channels sense the physical state of the bilayer (14–17). Nevertheless, given the critical role that lipid-protein interactions play in prokaryotic function (15), two questions arise: First, what is the correspondence between these crystal structures and mech-

anistically defined functional states? Second, what are the conformational rearrangements underlying the transitions along the gating pathway?

Functional, spectroscopic, and computational studies have shown that in the pentameric MscL, activation gating proceeds as a result of a large tilt of both transmembrane (TM) segments (14, 17, 18). Concerted helical rotation and tilting generate a large aqueous pore, much as in the iris of a camera lens. However, an equivalent gating mechanism is not as obvious in the case of MscS. With three TM segments arranged as a homoheptamer (12), the structural design of MscS is very different from that of MscL. Furthermore, although the MscL crystal structure appears to be a good representation of the closed conformation in its native environment (19, 20), the functional state represented by the MscS crystal structure (12, 13) has yet to be determined (21–26). Finally, in the presence of a sustained mechanical stimulus, MscS undergoes a desensitization/inactivation transition (22, 27, 28) that is not fully understood at the molecular level. Thus, although MscL and MscS respond to similar bilayer perturbations, the mechanism of transducing these forces might be different.

Electron paramagnetic resonance (EPR) measurements on a lipid-reconstituted closed state of MscS have provided direct evidence for a more compact TM domain arrangement than that seen in the crystal structure (21). In the closed conformation, the TM1 and TM2 segments realign 9° toward the normal of the membrane, allowing TM3 to further narrow the permeation path. We investigated how bilayer deformations trigger MscS opening. To this end, we used site-directed spin-labeling and EPR spectroscopy to monitor the structural rearrangements in all three MscS TM segments, relative to the MscS crystal structure (12, 13) and in comparison with our spectroscopic data on the closed state.

We used cone-shaped amphiphiles that modify the bilayer tension profile (7, 15, 29) to stabilize the open conformation of MscS (Fig. 1). As expected (22, 28, 30), application of a sustained negative pressure elicits the activation and subsequent inactivation of MscS (Fig. 1A). Even in the absence of an applied external pressure, perfusion with lysophosphatidylcholine (LPC) micelles elicited spontaneous MscS openings (Fig. 1B) that displayed single-channel properties identical to those activated by transbilayer pressure differences. Under these conditions, MscS channels can be continuously recruited by

sequential incorporation of LPC, until the membrane seal breaks. We found no evidence of an LPC-induced desensitization/inactivation. This fortuitous observation makes LPC a very useful tool for the investigation of MscS in its open conformation by spectroscopic approaches. At the same time, it suggests that LPC incorporation might be exerting bilayer perturbation forces that are different from those of the better-characterized transbilayer pressure difference (31, 32).

One hundred twenty-seven cysteine mutants (Fig. 2A), covering the N-terminal region and all TM segments (residues 2 to 128), were expressed, spin-labeled, and reconstituted into liposomes (21, 33). Each labeled mutant was activated by incorporation of LPC (25 mole %), and EPR spectroscopic measurements were carried out on both the closed (21) and LPC-open conformations. Changes in probe mobility were evaluated from line-shape differences (the inverse of the width in the central resonant line, ΔH_0^{-1}) and the accessibility to either the membrane lipid [O_2 collision frequency (I_{O_2})] or the aqueous environment [NI_{NiEdda}] from power saturation experiments (34). Figure 2B shows spectra from residues lining the permeation pathway [Lys¹⁰⁵→Cys¹⁰⁵ spin label (L105C-SL) to G113C-SL] (35). The complete EPR environmental data set for the TM domain (Fig. 2C) shows that the transition to the open state in MscS is accompanied by smaller structural changes than those seen in the pentameric MscL (14). This is not unexpected,

given the smaller single-channel conductance of MscS (in respect to MscL) and the fact that small intersubunit movements in the homoheptamer could generate the radial pore changes needed to support ion conduction.

Upon opening, both the N terminus and the TM1-TM2 loop reduce their accessibility to the polar agent NiEdda. Given that the overall α periodicity of TM1 and TM2 is preserved, the most parsimonious explanation for this change in accessibility is the partial tilting of the segments into the membrane (Fig. 2C, bottom). Although the central portion of TM1 (from positions I38C-SL to I44C-SL, Fig. 2C) did not show major changes in dynamics, TM2 and TM3 became more mobile, and TM2 in particular became more exposed to the lipids (Fig. 2C, middle). Residues in the TM3 helix that are fully buried and isolated from water and lipids in the closed conformation (21) show a periodic increase in NiEdda accessibility in the open state (Fig. 2C, bottom, and Fig. 3B). This suggests that TM3 moves away from the sevenfold symmetry axis and increases the diameter of the permeation pathway.

The location and extent of these conformational rearrangements can be visualized by mapping the differences between open- and closed-state data sets onto the recently refined MscS crystal structure (12, 13) or its closed-state model (21) (Fig. 3A). Mobility changes for the TM1 helix were largest at both of its ends (Fig. 3A and fig. S2), as would be expected from a downward tilting of the most peripheral of TM

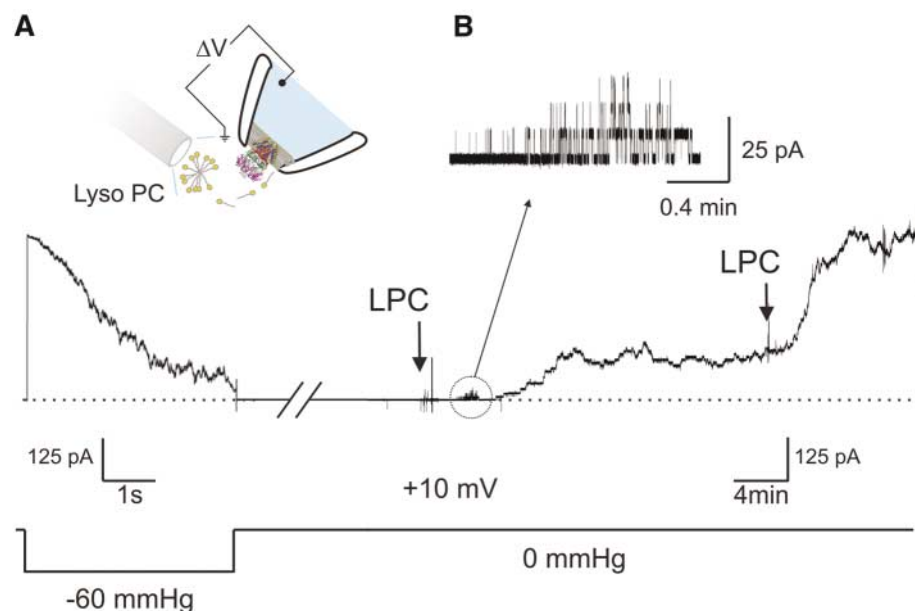


Fig. 1. LPC incorporation permanently activates MscS. (A) (Top) MscS orientation in the inside-out patch-clamp configuration and perfusion of LPC micelles. ΔV , transmembrane voltage; lyso PC, lysophosphatidylcholine. (Bottom) Representative MscS macroscopic currents (~ 55 channels in the patch) activated by negative pressure (at -60 mmHg and $+10$ mV) reveal the presence of a time-dependent inactivation process. (B) Sequential incorporation of LPC ($3 \mu M$) into the internal leaflet of inside-out patches from *Escherichia coli* spheroplasts and in the absence of applied tension elicits spontaneous openings (after ~ 2 min). All the channels present in the patch (as determined from tension-induced macroscopic currents) are activated by LPC. The inset shows single-channel transitions.

¹Department of Molecular Physiology and Biological Physics, University of Virginia, Charlottesville, VA 22908, USA. ²Department of Biochemistry and Molecular Biology, Institute for Biophysical Dynamics, University of Chicago, Chicago, IL 60637, USA. ³Howard Hughes Medical Institute and Department of Neurobiology, Harvard Medical School, Boston, MA 02115, USA. ⁴Department of Physics, University of Illinois at Urbana-Champaign, and Beckman Institute for Advanced Science and Technology, Urbana, IL 61801, USA.

*To whom correspondence should be addressed. E-mail: eperozo@uchicago.edu

segments. This rearrangement might represent the end effect of the transducing bilayer forces in the channel perimeter and would be in agreement with the suggestion that the tension sensor in MscS is located at both ends of the membrane/channel interface (6). Residues immediately preceding TM1 gained O₂ accessibility while simul-

taneously reducing NiEdda exposure (Fig. 3A). Mapping the TM1 and TM2 environmental changes onto the crystal structure revealed a better spatial correlation than when they were mapped onto the closed-state model (Fig. 3A). This might suggest that the crystal structure represents an intermediate gating conformation

more reminiscent of the open than the closed state (22–26).

After LPC incorporation, most of TM3 spin-labeled residues become more mobile and display a periodic increase (α -helical) in accessibility to NiEdda (Fig. 3B and fig. S4), as protein-protein contacts presumably weaken upon

Fig. 2. Structural rearrangements underlying channel opening. **(A)** A single MscS monomer is represented as part of the heptamer according to the MscS closed-state model obtained from the EPR-based refinement (21). The amino acid residues subjected to cysteine-scanning mutagenesis in the present study are shown as black spheres. **(B)** Representative X-band EPR spectra of consecutively spin-labeled mutants along the permeation pathway (TM3). Black and red traces were obtained from channels in the closed and open conformations, respectively. All spectra were obtained from samples at the same protein-to-lipid ratio, and a dielectric resonator with the microwave power set to 2 mW was used. Channel opening was obtained in dioleoylphosphatidylcholine:palmitoylphosphatidylglycerol + 25 mole % LPC vesicles. **(C)** Residue-specific environmental parameter profiles obtained in the open and closed (black curve) conformations for the N-terminal and TM segments: mobility parameter ΔH_0^{-1} (top, green curve), O₂ accessibility parameter ΠO_2 (middle, red curve), and NiEdda accessibility parameter $\Pi NiEdda$ (bottom, blue curve) are shown. The black horizontal bar covers the region for which EPR spectra are shown in (B). Gray areas represent the TM segment assignment derived from the MscS crystal structure (12, 13).

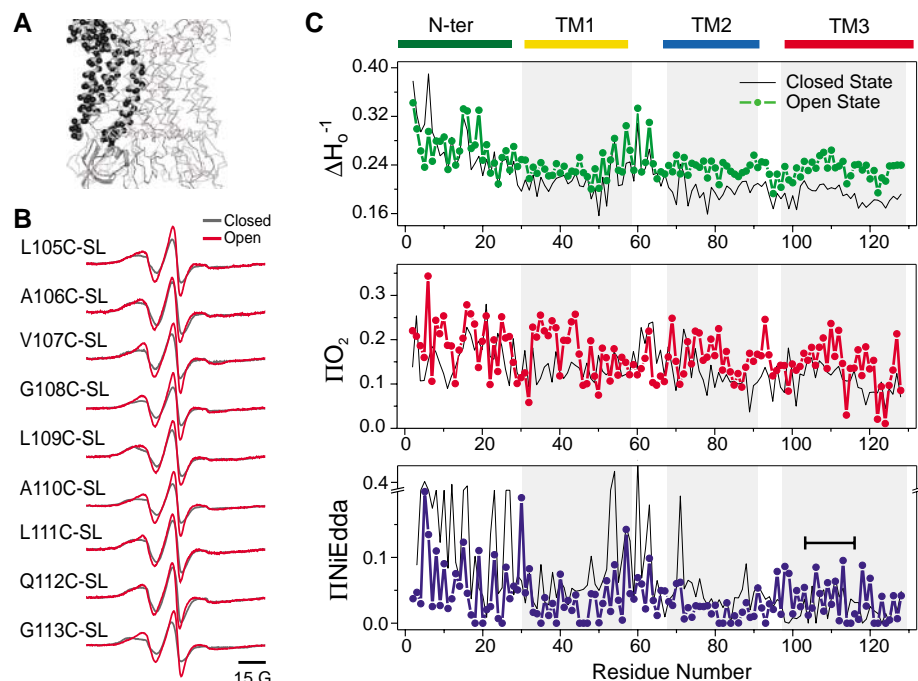
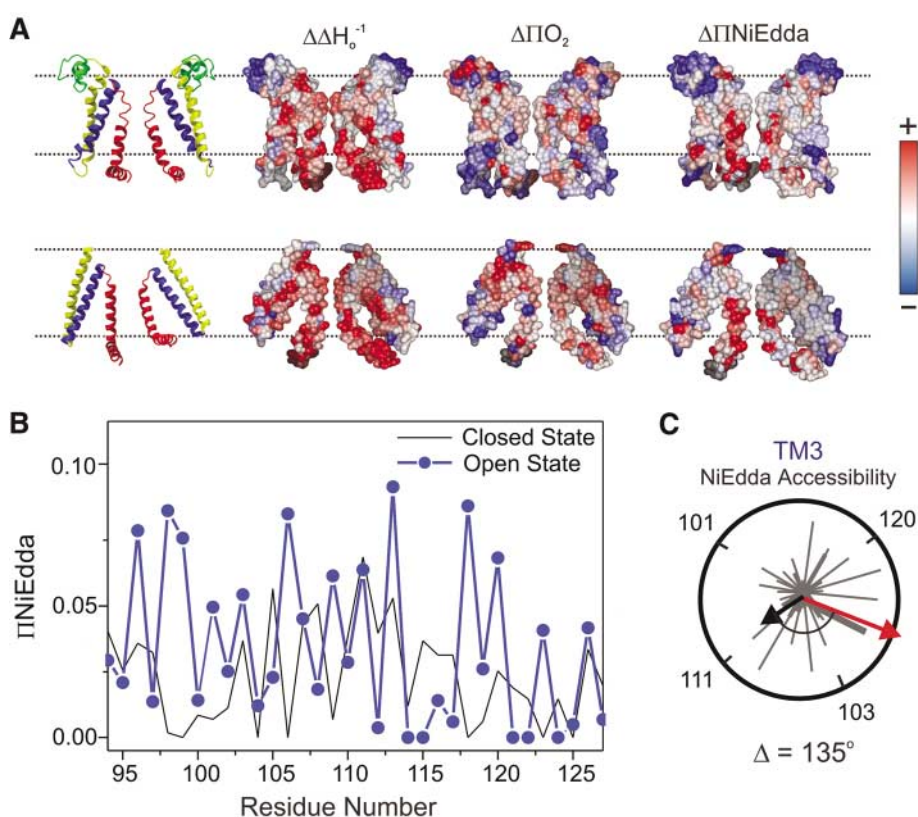


Fig. 3. Extent and direction of environmental parameter changes upon MscS opening. **(A)** Changes in local dynamics and solvent accessibilities mapped onto molecular surfaces of the closed-state EPR-based model (top) and the crystal structure (bottom). At left are ribbon representations of MscS (two subunits are shown for clarity), where individual TM segments are color-coded as follows: N terminus, green; TM1, yellow; TM2, blue; and TM3, red. From left to right, mobility ($\Delta\Delta H_0^{-1}$), oxygen accessibility ($\Delta\Pi O_2$), and NiEdda accessibility ($\Delta\Pi NiEdda$) changes are shown. **(B)** $\Pi NiEdda$ residue-specific environmental parameter profile for the TM3 helix obtained in the open (blue curve) and closed (black curve) conformations. **(C)** Vector analysis of TM3 environmental data in the open conformation. $\Pi NiEdda$ parameters have been superimposed in a polar coordinate. Resultant moments for the closed (black arrow) and open (red arrow) conformations were calculated from the accessibilities.



opening. When mapped in nonconducting models (Fig. 3A), the NiEdda-accessible face of the TM3 helix in the open state points away from the permeation pathway. This suggests that TM3 undergoes a substantial rotation about its principal axis. Moreover, the C-terminal part of TM3 also appears to face into the permeation pathway. This accessibility change would require at least some straightening of the two TM3 segment helices, because regions immediately after the G113 kink show no measurable NiEdda accessibility in the closed conformation (Fig. 3B). This experimental evidence agrees with previous molecular dynamics (MD) simulations (21, 23), as well as with an experimental study in which helical formation induced by G113A and G121A prevented inactivation and inactivation and closure, respectively (30).

The direction of the TM helices' movement can be deduced from changes in individual environmental moments between the closed and open states, as shown on a helical wheel representation (Fig. 3C and fig. S4). Calculation of the resultant angular vector differences shows that in order to explain the changes in O₂ accessibilities (A33C-SL to I39C-SL, and G41C-SL to I44C-SL), TM1 and TM2 segments must rotate about 50° and 36°, respectively, in the counterclockwise direction (fig. S5). Furthermore, to satisfy the changes in NiEdda accessibility data, the TM3 helices not only have to translate away from the symmetry axis but also need to rotate about 130° in the counterclockwise direction (Fig. 3C). Although the magnitude of the helix rotations reported might be biased by repacking of some of the spin-labeled mutants, the overall trend and direction of helix rotations (derived from the combination of data from multiple independent mutants) should not be affected. These movements provide a mechanistically feasible way to expose the helix face highlighted by residues A98C-SL, A106C-SL, and G113C-SL to the permeation pathway in the open state (Fig. 3B), while defining intersubunit contacts in the closed state. Such rotations would break a proposed hydrophobic seal responsible for stabilizing the seven-helix bundle in the closed state and serve as an energetic barrier to the ion flow (25, 36). Given the diameter of NiEdda (~6 Å) and the average length of the nitroxide tether (~5 Å), the diameter of the permeation path in the open conformation should be at least 11 Å to allow unfettered diffusion of the collisional contrast agent into the open pore (22, 30).

Using a computational approach that takes advantage of EPR-determined solvent accessibility restraints (37), we previously generated an EPR-based model of the closed state (21). In this work, we used this as a starting conformation to model a symmetrized version of the MscS open state. First, MscS TM helices were rotated according to the changes in helical environment moments obtained from the EPR data sets. Then, pseudo-atoms representing EPR spin-label probes were attached to residues 2 to 128. Finally, MD

simulations were performed in which interactions between EPR probes and pseudo-atoms representing NiEdda and O₂ were chosen to enforce the environments detected in the EPR experiments. In addition, an external cylindrical harmonic potential was applied to C α atoms to induce channel opening [see supporting online material (SOM) for details].

The resulting MscS open model that best satisfied our experimental constraints is shown in Fig. 4A. Comparison with the closed conformation suggests three key gating mechanistic highlights: (i) The TM1 helix tilts downward and rotates to expose TM2 to the membrane, and (ii) helices TM3a and TM3b move away from the permeation pathway, while (iii) TM3a inclines toward the plane of the bilayer, decreasing the kink angle at G113. Residue L105 (Fig. 4B), previously forming a putative hydrophobic seal, now faces away from the pore, and the narrowest part of the pore (about 11 Å in diameter) is lined by residue V99.

We have analyzed our current models of MscS closed and open conformations in light of the available experimental data. All-atom MD simulations of the open state (SOM) predict an ionic conductance that approximates the 1 nS seen experimentally (38). Furthermore, when some of the extreme mutations that cause either loss- or gain-of-function phenotypes (LOF or

GOF) are mapped on both the closed and open models, a strong spatial correlation emerges (Fig. 4B). In either conformation, LOF mutants tend to localize at the protein/membrane interface, whereas GOF mutants cluster in the middle of the TM segments. The location of the LOF mutants (6) might help explain their phenotype, because specific polar substitutions could strengthen interaction with lipid head groups, increasing the energetic cost of the TM1-TM2 hairpin tilting required for channel opening. On the other hand, polar GOF substitutions in the middle of TM1 and TM2 would affect interhelix packing, perhaps favoring the interhelix rearrangement between TM1 and TM2 (Fig. 4B) that leads to opening. Strong GOF phenotypes derived from mutations in the pore (39) destabilize the hydrophobic seal required to keep the channel closed and might promote TM3 rotation.

Vertical cross sections of the permeation pathway calculated (40) for the closed and open models and the refined MscS crystal structure (13) highlight the pore's morphological changes in the different structural snapshots during gating (Fig. 4C). The MscS crystal structure shows a narrow (~6 Å) region in the intracellular side of the pore that extends 10 Å in the z axis and has been associated with the formation of a non-conductive "vapor plug" (24–26). In our closed-state model (21), this narrowing extends 25 Å

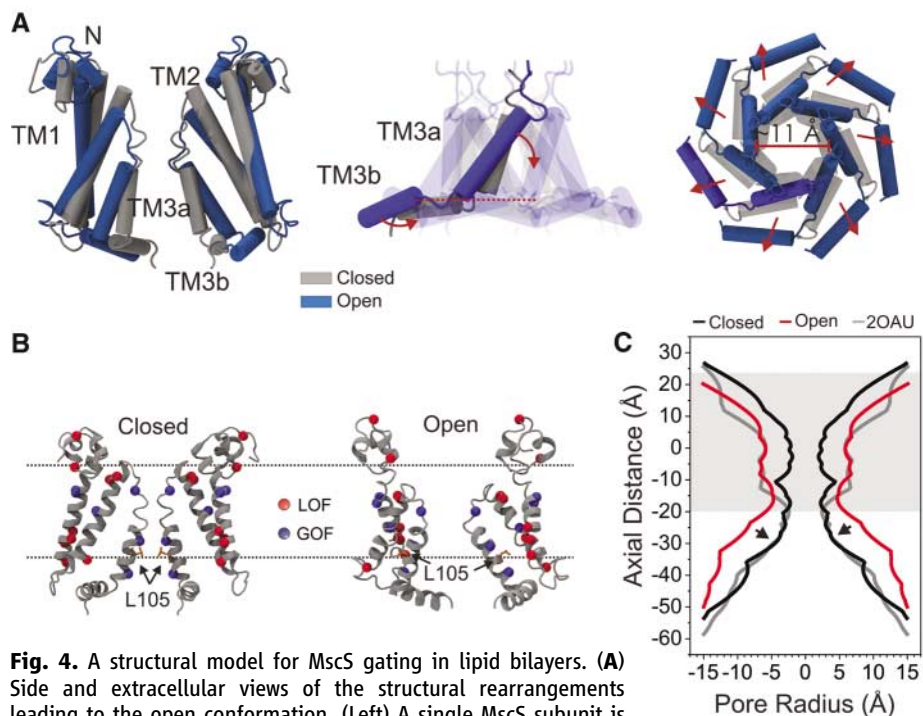


Fig. 4. A structural model for MscS gating in lipid bilayers. (A) Side and extracellular views of the structural rearrangements leading to the open conformation. (Left) A single MscS subunit is highlighted in blue and gray for the open and closed states, respectively. (Middle) TM3a and TM3b helices (residues 94 to 128 and 91 to 128 for the closed and open models, respectively). (Right) Extracellular view of the pore. Helical movements are illustrated by red arrows. (B) GOF (blue) and LOF (red) mutants mapped onto two subunits of MscS closed (left) and open (right) conformation models. GOF: I39N and I78N (6); V40D (41); and T93R, A102P, and L109S (39). LOF: V6C and A19C (21); I48D/S49P (39); and A51N, L55N, F68N, A85N, and L86N (6). Residue L105 (arrows) is shown in stick representation. (C) Cross-sectional area of the MscS pore in the closed, open, and crystal conformations. Each cross section was obtained from the calculated surface with the use of the program HOLE (40).

toward the extracellular side of the pore, further increasing the energetic cost for ions to traverse this region. The series of TM1-TM2 tilts and TM3 rotations leads to the formation of a large 10 to 12 Å × 20 Å conductive pathway lined by the TM3a and TM3b segments; preliminary MD simulations show conduction of both cations and anions through this pore (fig. S6). These permeation pathway cross sections underlie the similarities between the open model and the MscS crystal structure (12, 13). Except for the narrowing at the intracellular end of its pore (Fig. 4C, arrows), the crystal structure could, in principle, support ion conduction and thus might represent an inactivated/desensitized conformation after opening. The structural rearrangements described here demonstrate a gating mechanism that is distinct from that of MscL (14, 17, 18) but confirms the critical role of helix tilting in transducing bilayer deformations to generate an aqueous pathway through the membrane.

Note added in proof: A recent model of open MscS (42), based on computation and single-channel analyses, is in agreement with the present conformation of TM3 (Fig. 2).

References and Notes

- N. Levina *et al.*, *EMBO J.* **18**, 1730 (1999).
- A. P. Christensen, D. P. Corey, *Nat. Rev. Neurosci.* **8**, 510 (2007).
- B. Martinac, *Cell. Physiol. Biochem.* **11**, 61 (2001).
- C. D. Pivetti *et al.*, *Microbiol. Mol. Biol. Rev.* **67**, 66 (2003).
- K. Yoshimura, T. Nomura, M. Sokabe, *Biophys. J.* **86**, 2113 (2004).
- T. Nomura, M. Sokabe, K. Yoshimura, *Biophys. J.* **91**, 2874 (2006).
- F. Maingret, A. J. Patel, F. Lesage, M. Lazdunski, E. Honore, *J. Biol. Chem.* **275**, 10128 (2000).
- K. Hayakawa, H. Tatsumi, M. Sokabe, *J. Cell Sci.* **121**, 496 (2008).
- P. Gottlieb *et al.*, *Pflugers Arch.* **455**, 1097 (2008).
- K. Y. Kwan *et al.*, *Neuron* **50**, 277 (2006).
- G. Chang, R. H. Spencer, A. T. Lee, M. T. Barclay, D. C. Rees, *Science* **282**, 2220 (1998).
- R. B. Bass, P. Strop, M. Barclay, D. C. Rees, *Science* **298**, 1582 (2002).
- S. Steinbacher, R. Bass, P. Strop, D. C. Rees, *Structures of the Prokaryotic Mechanosensitive Channels MscL and MscS* (Current Topics in Membranes. Mechanosensitive Ion Channels, Part A, Elsevier, New York, 2007), pp. 1–24.
- E. Perozo, D. M. Cortes, P. Sompornpisut, A. Kloda, B. Martinac, *Nature* **418**, 942 (2002).
- E. Perozo, A. Kloda, D. M. Cortes, B. Martinac, *Nat. Struct. Biol.* **9**, 696 (2002).
- S. Sukharev, M. Betanzos, C. S. Chiang, H. R. Guy, *Nature* **409**, 720 (2001).
- J. Gullingsrud, K. Schulten, *Biophys. J.* **85**, 2087 (2003).
- M. Betanzos, C. S. Chiang, H. R. Guy, S. Sukharev, *Nat. Struct. Biol.* **9**, 704 (2002).
- E. Perozo, A. Kloda, D. M. Cortes, B. Martinac, *J. Gen. Physiol.* **118**, 193 (2001).
- J. Gullingsrud, D. Kosztin, K. Schulten, *Biophys. J.* **80**, 2074 (2001).
- V. Vasquez *et al.*, *J. Mol. Biol.* **378**, 55 (2008).
- M. Sotomayor, V. Vasquez, E. Perozo, K. Schulten, *Biophys. J.* **92**, 886 (2007).
- M. Sotomayor, T. A. van der Straaten, U. Ravaioli, K. Schulten, *Biophys. J.* **90**, 3496 (2006).
- M. Sotomayor, K. Schulten, *Biophys. J.* **87**, 3050 (2004).
- A. Anishkin, S. Sukharev, *Biophys. J.* **86**, 2883 (2004).
- S. A. Spronk, D. E. Elmore, D. A. Dougherty, *Biophys. J.* **90**, 3555 (2006).
- P. Koprowski, A. Kubalski, *J. Membr. Biol.* **164**, 253 (1998).
- A. Akitake, A. Anishkin, S. Sukharev, *J. Gen. Physiol.* **125**, 143 (2005).
- B. Martinac, J. Adler, K. Kung, *Nature* **348**, 261 (1990).
- B. Akitake, A. Anishkin, N. Liu, S. Sukharev, *Nat. Struct. Mol. Biol.* **14**, 1141 (2007).
- P. Moe, P. Blount, *Biochemistry* **44**, 12239 (2005).
- V. S. Markin, F. Sachs, in *Thermodynamics of Mechanosensitivity*, O. Hamill, Ed. (Current Topics in Membranes. Mechanosensitive Ion Channels, Part A. Elsevier, New York, 2007), pp. 87–119.
- V. Vasquez, D. M. Cortes, H. Furukawa, E. Perozo, *Biochemistry* **46**, 6766 (2007).
- Z. T. Farahbakhsh, C. Altenbach, W. L. Hubbell, *Photochem. Photobiol.* **56**, 1019 (1992).
- Single-letter abbreviations for the amino acid residues are as follows: A, Ala; C, Cys; D, Asp; E, Glu; F, Phe; G, Gly; H, His; I, Ile; K, Lys; L, Leu; M, Met; N, Asn; P, Pro; Q, Gln; R, Arg; S, Ser; T, Thr; V, Val; W, Trp; and Y, Tyr.
- M. D. Edwards *et al.*, *Nat. Struct. Mol. Biol.* **12**, 113 (2005).
- P. Sompornpisut, E. Perozo, B. Roux, *Biophys. J.* *BioFAST*, 10.1529/biophysj.108.142984 (2008).
- B. Martinac, M. Buechner, A. H. Delcourt, J. Adler, C. Kung, *Proc. Natl. Acad. Sci. U.S.A.* **84**, 2297 (1987).
- S. Miller *et al.*, *EMBO J.* **22**, 36 (2003).
- O. S. Smart, J. G. Neduveitil, X. Wang, B. A. Wallace, M. S. Sansom, *J. Mol. Graphics* **14**, 354 (1996).
- K. Okada, P. C. Moe, P. Blount, *J. Biol. Chem.* **277**, 27682 (2002).
- A. Anishkin *et al.*, *J. Gen. Physiol.* **132**, 67 (2008).
- We thank V. Jogini, S. Chakrapani, H. Raghuraman, and D. M. Cortes for providing comments and experimental advice and G. R. Meyer for EPR data analysis script. M.S. is an associate of the Howard Hughes Medical Institute in the laboratory of David Corey. This work was supported by NIH grants GM063617 (E.P.), P41-RR05969 (K.S.), and 1 R01 GM067887 (K.S.). Supercomputer time was provided through NSF grant LRAC MCA935028.

Supporting Online Material

www.sciencemag.org/cgi/content/full/321/5893/1210/DC1
Materials and Methods
Figs. S1 to S6
Table S1
References

28 April 2008; accepted 31 July 2008
10.1126/science.1159674

Pre-Columbian Urbanism, Anthropogenic Landscapes, and the Future of the Amazon

Michael J. Heckenberger,^{1*} J. Christian Russell,² Carlos Fausto,³ Joshua R. Toney,⁴ Morgan J. Schmidt,⁵ Edithe Pereira,⁶ Bruna Franchetto,⁷ Afukaka Kuikuro⁸

The archaeology of pre-Columbian polities in the Amazon River basin forces a reconsideration of early urbanism and long-term change in tropical forest landscapes. We describe settlement and land-use patterns of complex societies on the eve of European contact (after 1492) in the Upper Xingu region of the Brazilian Amazon. These societies were organized in articulated clusters, representing small independent polities, within a regional peer polity. These patterns constitute a “galactic” form of prehistoric urbanism, sharing features with small-scale urban polities in other areas. Understanding long-term change in coupled human-environment systems relating to these societies has implications for conservation and sustainable development, notably to control ecological degradation and maintain regional biodiversity.

Are there “lost cities” in the Amazon that await discovery in the dense tropical forests of the region? If so, how did indigenous civilizations alter forested environments, and do past patterns provide clues to resource management today? Recent archeology, which documents large settlements (>30 ha) and extensive landscape alterations in several areas,

has sparked debate on prehistoric Amazonian urbanism (Fig. 1A) (1–3). The Upper Xingu region of the southern Amazon (Mato Grosso, Brazil) is one critical example of complex settlement and land-use patterns (4–6). Here, we report recent findings on settlement planning and supralocal integration, which document a highly self-organized anthropogenic landscape of late

prehistoric towns, villages, and hamlets, with well-planned road networks across the region. These patterns, although differing substantially from other world areas, share characteristics common of small, urban polities elsewhere.

The nature and development of prehistoric urbanism are contested issues. In recent decades, archaeological and historical studies of non-Western cases across the globe have emphasized variability, in addition to central-place and city-state forms, and substantially expanded the known distribution of urban societies [supporting online material (SOM) text] (7–9). Early urban societies are characterized by a “reasonably large and permanent concentration of people within a limited territory” but are commonly “identified with a broad-type of ritual-political centre... with small residential populations and are thus ‘marginally urban’” (10, 11). We use a definition of early urbanism that is not limited to cities, meaning megacenters (5000 or more persons) distinctive in form and function from rural or suburban communities, but that also includes multicentric networked settlement patterns, including smaller centers or towns.

Rather than ancient cities, complex settlement patterns in the Upper Xingu were characterized by a network of permanent plaza communities integrated in territorial polities (~250 km²). This